# - Supplementary Information - Exciton annihilation and diffusion length in disordered multichromophoric nanoparticles

Amira Mounya Gharbi[1], Deep Sekhar Biswas[2], Olivier Crégut[1], Pavel Malý[3], Pascal Didier[2], Andrey Klymchenko[2], and Jérémie Léonard[*1]

[1]IPCMS, Université de Strasbourg - CNRS, Strasbourg, France
[2]LBP, Université de Strasbourg, Illkirch, France
[3]Charles University, Prague, Czech Republic

## Table of content

**1 Modeling the exciton decay kinetics inside nanoparticles 2**

**2 Averaging the decay kinetics over the detection volume 4**
2.1 Initial exciton density across the excitation volume . . . 4
2.2 Detected fluorescence decay kinetics . . . 6
2.3 Integration along $z$ . . . 6
2.4 The flat excitation profile or detection through a pinhole . . . 8
2.5 The Gaussian pulse profile . . . 8
2.6 Finite pinhole size . . . 10
2.7 Graphical illustrations . . . 11

**3 Time-resolved fluorescence acquisition and data processing 13**
3.1 Experimental conditions . . . 13
3.2 Measuring the laser spot section at the sample location . . . 14
3.3 Testing the linear regime of rhodamine dye excitation . . . 16
3.4 Data acquisition and processing . . . 16
3.5 Signal absolute calibration in units of exciton density in the ONP's. . . . 18

**4 Complementary time-resolved fluorescence data 20**

[*]Corresponding author: jeremie.leonard@ipcms.unistra.fr

**5 Modeling the light-induced formation of a quencher species** **21**

**6 Förster radius $R_0$ for homo-FRET** **22**

**7 Transient absorption spectroscopy and Förster radius for EEA** **23**

**8 Pulsed versus cw illumination** **25**

# 1 Modeling the exciton decay kinetics inside nanoparticles

**Note:** As additional supplementary material, we provide python routines available at this link [1], which implement the model functions introduced below and their fit to the data disclosed in the main text.

### Solving the rate equation for mono- and bi- molecular decay

The variation of the exciton ($S_1$ electronic state) density $\frac{dn(t)}{dt}$ due to exciton-exciton annihilation (EEA), or singlet-singlet annihilation (SSA) is defined as $-\gamma(t)n^2(t)$. SSA produces one electonic ground state $S_0$, and one higher-lying electronic state $S_p$ ($p > 1$), thus corresponding to the loss of two excitons. In general the $S_p$ state is very short lived and ultrafast internal conversion occurs which converts $S_p$ back to $S_1$, such that one out of 2 excitons is reformed almost instantaneously resulting in an exciton density growth with rate $+1/2\gamma(t)n^2(t)$. In this case, the exciton density $n(t)$ evolves - in each nanoparticle - according to:

$$\frac{dn(t)}{dt} = -kn(t) - \frac{1}{2}\gamma(t)n^2(t), \tag{1}$$

where $k$ is the (time-independent) fluorescence decay rate of an isolated exciton, and $\gamma(t)$ the SSA rate, which is assumed to be time dependent in the general case. Equation 1 is easily time-integrated by changing variable to $v = 1/n$, since:

$$\frac{dv}{dt} = -\frac{1}{n^2}\frac{dn}{dt} = \frac{1}{n^2}(kn + \frac{\gamma}{2}n^2) \quad \Rightarrow \quad \frac{dv}{dt} - kv = \frac{\gamma}{2} \tag{2}$$

The solution of the homogeneous equation $\frac{dv}{dt} - kv = 0$ is $v = C\exp(kt)$. A particular solution of the inhomogeneous equation can be obtained by the method of variation of parameters, i.e. by seeking a solution $v_1(t) = h(t)\exp(kt)$ ($h(t)$ has units of a volume, e.g. $cm^3$):

$$\begin{aligned}
\frac{dv_1}{dt} - kv_1 = \gamma(t) \quad \Rightarrow \quad & (h' + kh)\exp(kt) - kh\exp(kt) = \frac{\gamma(t)}{2} \\
& h'(t)\exp(kt) = \frac{\gamma(t)}{2} \quad \Rightarrow \quad h(t) = \int_0^t \frac{\gamma(u)}{2}\exp(-ku)du \\
& (h(t=0) = 0)
\end{aligned}$$

The general solution is thus $v = (C + h(t))\exp(kt)$. With initial condition $v(0) = 1/n_0$, we get:

$$v = 1/n(t) = (1/n_0 + h(t))\exp(kt)$$
$$i.e. \quad \frac{\exp(-kt)}{n(t)} = \frac{1}{n_0} + h(t) \quad \text{(used in ref. [2] )}$$

$$\boxed{n(t) = \frac{n_0\ \exp(-kt)}{1 + n_0\, h(t)}} \tag{3}$$

**The case of time-independent $\gamma$**

When $\gamma(t) = \gamma$ is constant, then we can define a characteristic exciton density $n_A = 2k/\gamma$ above which the term $\gamma n^2(t)/2$ dominates over $kn(t)$ in Eq. 1. Figure S1 illustrates the decay kinetics predicted by Eq. 3 for various values of $n_0$ expressed in units of $n_A$: For $n_0 \ll n_A$ the decay kinetics is monoexponential (i.e. no SSA) and does not depend on $n_0$. For $n_0 > n_A$ the early-time decay strongly accelerates due to SSA until $n(t)$ reaches values lower than $n_A$.

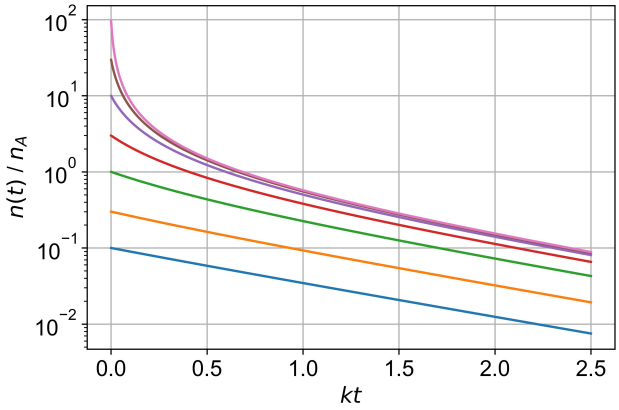


Figure S1: Exciton decay kinetics as predicted by Eq. 3 with time-independent $\gamma$, with $n_0$ values increasing from $n_A/10$ to $100\, n_A$.

With time-independent $\gamma$, we get $h(t) = \dfrac{k}{n_A}\displaystyle\int_0^t \exp(-ku)du = \frac{1}{n_A}(1 - \exp(-kt))$. Defining $\tau = kt$, we have:

$$h(\tau) = \frac{1}{n_A}(1 - \exp(-\tau)). \tag{4}$$

**The Gösele model for time-dependent $\gamma(t)$**

Although all our data are nicely fitted with time-independent $\gamma$ due to the large diffusion constant (see the main text), for completeness we also mention here the case of time-dependent $\gamma(t)$, commonly discussed (see e.g. ref [3]) based on the expression provided by Gösele et al. (see Eq. 24 of ref. [4], where we replace $D = D_A + D_D$ by $2D$ since both colliding excitons diffuse with diffusion constant $D$, as discussed in the main text):

$$\gamma(t) = 8\pi D R_e \, (1 + R_e/(2\pi D t)^{1/2}),$$

where $D$ is the exciton diffusion constant and $R_e$ is an effective exciton interaction radius. Introducing again $n_A = 2k/\gamma$, with $\gamma = 8\pi D R_e$, we get:

$$\gamma(t) = \frac{2k}{n_A} \left(1 + \frac{\sqrt{2\, n_A R_e^3}}{\sqrt{kt}}\right)$$

With $\tau = kt$, we then have:

$$h(\tau) = \frac{1}{n_A} \left(1 - \exp(-\tau) + \sqrt{2\pi\, n_A R_e^3}\, \mathrm{erf}(\sqrt{\tau})\right), \tag{5}$$

# 2 Averaging the decay kinetics over the detection volume

When focusing a laser spot in a solution of ONP's dispersed in water, the ONP's located in the pulse center where the laser intensity is larger have higher initial exciton density and possibly faster non-exponential decay kinetics if SSA occurs, than the ONP's located in the pulse periphery where the laser intensity and initial exciton density are lower and the decay kinetics remains monoexponential. The fluorescence decay kinetics actually observed is therefore the sum of all these contributions over the entire excitation (or detection, see below) volume.

## 2.1 Initial exciton density across the excitation volume

Consider a collimated ultrashort light pulse of total energy $\mathcal{E}_0$, with transverse energy profile $f(x, y)$, and propagating along the $z$ axis though an absorbing medium characterized by its absorption coefficient $a$, see Fig. S2. The pulse energy profile $\mathcal{E}(x, y, z)$ can be written:

$$\mathcal{E}(x, y, z) = \frac{\mathcal{E}_0}{S}\, e^{-az} f(x, y) \tag{6}$$

with $S$ the characteristic section of the laser pulse defined by $\int f(x, y) dx dy = S$ (normalization convention). The assumption that the transverse beam profile $f(x, y)$ does not depend on $z$ remains valid at the beam focus, provided that the Rayleigh range is longer than the sample thickness or light penetration depth.

Note: The Beer-Lambert law is commonly written in terms of the optical density $a' = a/\ln(10)$ such that $e^{-az} = e^{-\ln(10)\, a' z} = 10^{-a' z}$. If the sample is characterized by a uniform

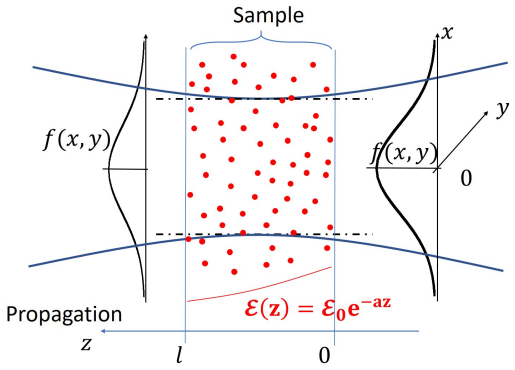


Figure S2: Propagation along $z$ axis and absorption of a pulse of transverse profile $f(x, y)$, focused in the sample.

concentration $c$ (in M) of absorbers, then $a'/c = \varepsilon$ is the extinction coefficient (in /M/cm) of the absorbers.

The number $dN$ of photons of energy $h\nu$ absorbed by an infinitesimal volume $dV = dxdydz$ centered at $\vec{r}$ inside the excitation volume is given by the pulse energy loss $d\mathcal{E}$ in that elementary volume:

$$\mathcal{E}(x, y, z + dz)dxdy - \mathcal{E}(x, y, z)dxdy = \frac{\partial \mathcal{E}}{\partial z} dV = -h\nu dN \tag{7}$$

$$\frac{dN}{dV}(x, y, z) = a \frac{\mathcal{E}_0}{S\, h\nu} f(x, y)\, e^{-az} \tag{8}$$

Within the linear regime of excitation - i.e. low (e.g. few %) excitation probability - each photon absorbed produces one exciton in the sample. If the medium uniformly absorbs (e.g. homogeneous film), then the initial exciton density produced by the laser pulse in $\vec{r}$ is:

$$n(\vec{r}; t = 0) = \frac{dN}{dV}(x, y, z) \tag{9}$$

$$n(\vec{r}; t = 0) = n_0\ f(x, y)\, e^{-az} \tag{10}$$

$$\text{with} \quad n_0 = a \frac{\mathcal{E}_0}{S\, h\nu}, \tag{11}$$

where $n_0$ is the initial peak exciton density at the sample surface ($z = 0$) and laser pulse center ($x = y = 0$).

Here however, the photons are absorbed by dyes encapsulated in nanoparticules dispersed in a dilute solution. With $\varepsilon$ the extinction coefficient of the dyes in the ONP's, $c = a'/\varepsilon = a/(\varepsilon \ln(10))$ is the apparent average dye concentration in the solution, much lower than the actual dye concentration within ONP's. The dye excitation probability $\mu$ is the ratio between the number of absorbed photons $dN$ and the number of dyes in the voulme $dV$ : $\mu = dN/(dV \times c\, N_A)$, with

$N_A$ the Avogadro number:

$$\mu(x,y,z) = \frac{dN}{dV}(x,y,z)\frac{\varepsilon \ln(10)}{aN_A} \tag{12}$$

$$\mu(x,y,z) = \frac{\varepsilon \ln(10)}{N_A\, h\nu}\frac{\mathcal{E}_0}{S}\, f(x,y)\, e^{-az} \tag{13}$$

Hence, the initial exciton density created inside ONP's located in $\vec{r}$ is :

$$n(\vec{r}; t=0) = \mu(x,y,z) \times \rho, \tag{14}$$

where $\rho$ is the dye number density in the ONP. Therefore we write:

$$\boxed{\begin{aligned} n(\vec{r}; t=0) &= n_0\ f(x,y)\, e^{-az} \\ \text{with} \qquad n_0 &= \rho\, \frac{\varepsilon \ln(10)}{N_A}\frac{\mathcal{E}_0}{S\, h\nu} \end{aligned}} \tag{15}$$

### 2.2 Detected fluorescence decay kinetics

The fluorescence emission at a location $\vec{r}$ within the excitation volume is proportional to the local exciton population $n(\vec{r}, t)$, which decays according to Eq. 3, starting from the initial exciton density $n(\vec{r}; t=0)$ given by Eq. 15. Hence the total fluorescence signal measured is proportional to the integral $F(t)$ of $n(\vec{r}, t)$ over the entire detection volume $V$:

$$F(t) = \frac{1}{V}\int \frac{n_0\, e^{-az} f(x,y)\ \exp(-kt)}{1 + n_0\, e^{-az} f(x,y)\, h(t)} d\vec{r} \tag{16}$$

### 2.3 Integration along *z*

We define:

$$F(t) = \frac{1}{S}\int G(x,y,t)\ dxdy\ , \tag{17}$$

$$\text{with} \quad G(x,y,t) = \frac{1}{l}\int_0^l \frac{n_0\, e^{-az} f(x,y)\ \exp(-kt)}{1 + n_0\, e^{-az} f(x,y)\, h(t)} dz, \tag{18}$$

and compute, with $\alpha = n_0\ \exp(-kt)\, f(x,y)$, and $\beta = n_0\, h(t)\, f(x,y)$:

$$G(x,y,t) = \frac{1}{l}\int_0^l \frac{\alpha e^{-az}}{1 + \beta\, e^{-az}} dz \tag{19}$$

$$= -\frac{\alpha}{al}\int_1^{e^{-al}} \frac{du}{1+\beta\, u} \quad \text{with} \quad u = e^{-az}, \quad du = -audz \tag{20}$$

$$= \frac{-\alpha}{\beta al}\left[\ln(1+\beta u)\right]_1^{e^{-al}} = \frac{\alpha}{\beta al}\ln\left(\frac{1+\beta}{1+\beta e^{-al}}\right) \tag{21}$$

$$G(x,y,t) = \frac{1}{al}\frac{\exp(-kt)}{h(t)}\ln\left(\frac{1 + n_0\, h(t)\, f(x,y)}{1 + n_0\, h(t)\, f(x,y) e^{-al}}\right), \tag{22}$$

where $e^{-al} = 10^{-A}$, with $A$ the sample absorbance at the excitation wavelength ($al = A\ln(10)$).

**Column- or $z$- averaged exciton density**

As we will see below, it is useful to define $\tilde{n}_0$ the average of the initial peak exciton density $n(x=y=0,z;t=0)$ along the $z$ axis over the sample thickness:

$$\tilde{n}_0 = \frac{1}{l}\int_0^l n(x=y=0,z;t=0)dz = \frac{1}{l}\int_0^l n_0\, e^{-az}dz \tag{23}$$

$$i.e. \quad \tilde{n}_0 = n_0 \times \frac{1-e^{-al}}{al} = n_0 \times \frac{1-10^{-A}}{A\ln(10)} \tag{24}$$

with $A = al/\ln(10)$, the sample absorbance.

For opaque samples ($e^{-al}=0$), $\tilde{n}_0 = \dfrac{n_0}{al} = \dfrac{n_0}{A\ln(10)}$.

For weakly absorbing samples, one can define $u = al < 1$ and write:

$$\tilde{n}_0 \simeq n_0 \frac{1-(1-u+u^2/2)}{u} \tag{25}$$

$$\tilde{n}_0 = n_0(1-u/2+O(u^2)) \tag{26}$$

$$\text{or equivalently} \quad n_0 = \tilde{n}_0(1+u/2+O(u^2)) \tag{27}$$

**Weakly absorbing samples**

We now write $G(x,y,t)$ (Eq. 22) as a function of $\tilde{n}_0$ rather than $n_0$. With $u = al$ (i.e. $u = A\ln(10)$, with $A$ the sample absorbance), we have:

$$n_0\, e^{-al} = n_0\, e^{-u} = n_0 - u\,\tilde{n}_0$$

$$\text{such that} \quad \frac{1+n_0\,h(t)\,f(x,y)e^{-al}}{1+n_0\,h(t)\,f(x,y)} = \frac{1+hf\,(n_0-u\,\tilde{n}_0)}{1+hf\,n_0} = 1-\frac{u\tilde{n}_0\,hf}{1+n_0hf}$$

Hence for $u<1$, using Eq. 27, we get:

$$\begin{aligned}
\frac{1+n_0\,h(t)f(x,y)\,e^{-al}}{1+n_0\,h(t)f(x,y)} &= 1-\frac{uhf\tilde{n}_0}{1+hf\tilde{n}_0(1+u/2+O(u^2))} \\
&= 1-\alpha u(1-\alpha u/2+O(u^2)), \quad \text{with} \quad \alpha = \frac{hf\tilde{n}_0}{1+hf\tilde{n}_0} < 1 \\
&= 1-\alpha u+\alpha^2u^2/2+O(u^3), \\
\frac{1}{u}\ln\left(\frac{1+n_0\,h(t)f(x,y)}{1+n_0\,h(t)f(x,y)\,e^{-u}}\right) &= \frac{-1}{u}\left(-\alpha u+\alpha^2u^2/2-\alpha^2u^2/2+O(u^3)\right) \\
&= \alpha+O(u^2)
\end{aligned}$$

Here it is important to notice in the last equality, that the term linear in $u$ cancels out, such that

$$G(x,y,t) = \frac{\tilde{n}_0 f(x,y)\exp(-kt)}{1+\tilde{n}_0 f(x,y)h(t)} \tag{28}$$

**is correct up to second order in $u = al$, and is therefore an excellent approximation of Eq.18 in the case of weakly absorbing samples ($u < 1$).**

### 2.4 The flat excitation profile or detection through a pinhole

Assume we excite the sample with a flat-top pulse shape, that is $f(x,y) = 1$ across the pulse section $S$ and $f(x,y) = 0$ outside. Alternatively, we may excite the sample with a non flat laser pulse, but detect only the fluorescence emitted form the central part of the excitation volume (where the excitation energy is close to uniform in the transverse direction, i.e. $f(x,y) \simeq 1$), by using a pinhole in a confocal fluorescence collection scheme, as illustrated in Figure 2 in the main text. In both cases, the integration on $x, y$ becomes trivial:

$$F(t) = \frac{1}{al}\,\frac{\exp(-kt)}{h(t)}\,\ln\left(\frac{1+n_0\,h(t)}{1+n_0\,h(t)e^{-al}}\right) \tag{29}$$

$$\boxed{F(t) = \frac{\tilde{n}_0\exp(-kt)}{1+\tilde{n}_0 h(t)} \quad (\text{for } al < 1)} \tag{30}$$

Notice that Eq. 30 is nothing but Eq. 3 where we replace $n_0$ by $\tilde{n}_0$.

### 2.5 The Gaussian pulse profile

Assuming a Gaussian pulse energy profile (with $f(0,0) = 1$), we define:

$$f(x,y) = \exp\left(-\frac{x^2}{w_1^2} - \frac{y^2}{w_2^2}\right), \quad \text{with} \quad \int f(x,y)dxdy = \pi w_1 w_2 = S \tag{31}$$

In the expression for the fluorescence signal $F(t) = \frac{1}{S}\int G(x,y,t)\;dxdy$ , with $G(x,y,t)$ as given by Eq. 22, we have integrals of the form:

$$J = \frac{1}{S}\int \ln\left(1+\beta\,\exp\left(-\frac{x^2}{w_1^2} - \frac{y^2}{w_2^2}\right)\right)dxdy \tag{32}$$

$$= \frac{w_1 w_2}{S}\int_0^\infty \ln\left(1+\beta\,e^{-r^2}\right)\,2\pi r dr, \quad \text{with} \quad r^2 = \frac{x^2}{w_1^2} + \frac{y^2}{w_2^2} \tag{33}$$

$$= -\int_{-\beta}^{0} \ln(1-u)\;\frac{du}{u}, \quad \text{with} \quad u = -\beta\,e^{-r^2}, \quad du = -2r\,u dr \tag{34}$$

$$= -Li_2(-\beta), \tag{35}$$

where, $Li_2(z)$ is the dilogarithm function as defined in ref. [5]:

$$Li_2(z) = -\int_0^z \ln(1-u)\frac{du}{u} = \sum_{n=1}^{\infty}\frac{z^n}{n^2} \tag{36}$$

We conclude, that with a Gaussian laser pulse profile, the **detected fluorescence** decay kinetics is given by:

$$F(t) = \frac{\exp(-kt)}{h(t)\,al}\ \left(-Li_2(-n_0h(t)) + Li_2(-n_0h(t)e^{-al})\right) \tag{37}$$

Here we note, that assuming an **opaque sample**, **i.e.** $e^{-al} = 0$ , we get the result already derived by Kirm et al.: [6]

$$F(t) = \frac{\exp(-kt)}{h(t)\,A\ln(10)}\ (-Li_2(-n_0h(t))) \tag{38}$$

**Weakly absorbing samples**

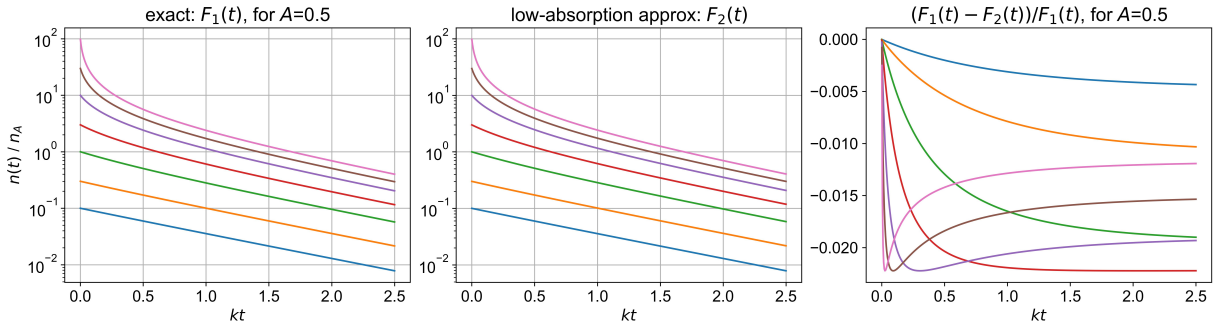


Figure S3: Fluorescence decay kinetics observed upon integration over the entire Gaussian transverse profile and sample thickness: Comparison between the "exact" expression $F_1(t)$ given by Eq. 37, and the "low-absorption" approximation $F_2(t)$ given by Eq. 39. We see, that even for an absorbance A=0.5, the approximation is correct to $\sim 2\%$ in relative values, whatever the initial exciton density. The relative error increases to no more than $\sim 8\%$ for A=1, and reduces to $< 0.1\%$ when $A < 0.1$ as in all experiments reported in the main text.

We now compute the fluorescence signal $F(t) = \frac{1}{S}\int G(x,y,t)\ dxdy$ , with $G(x,y,t)$ as given by Eq. 28:

$$F(t) = \frac{1}{S}\exp(-kt)\int \frac{\tilde{n}_0\, f(x,y)}{1+\tilde{n}_0\, h(t)\, f(x,y)}\; dxdy$$
$$= \frac{w_1 w_2}{S}\;\exp(-kt)\int_0^\infty \frac{\tilde{n}_0\, e^{-r^2}}{1+\tilde{n}_0\, h(t)\, e^{-r^2}}\; 2\pi r dr, \quad \text{with} \quad r^2 = \frac{x^2}{w_1^2}+\frac{y^2}{w_2^2}$$
$$F(t) = -\frac{\exp(-kt)}{h(t)}\int_{\tilde{n}_0 g}^0 \frac{du}{1+u}, \quad \text{with} \quad u = \tilde{n}_0 h(t)\, e^{-r^2}, \quad du = -2r\, u dr$$

$$\boxed{F(t) = \frac{\exp(-kt)}{h(t)}\ln(1+\tilde{n}_0 h(t))} \tag{39}$$

In the case $\gamma(t) = \gamma$ is time-independent, Figure S3 compares the decay kinetics expected after integration over the excitation volume according to the exact expression Eq.37 or to the low-absorption approximation Eq. 39, for a sample absorbance $A = 0.5$, corresponding to $al$ as large as $al = 0.5 \times \ln(10) \sim 1.15$.

### 2.6 Finite pinhole size

We now assume that the pinhole is not "small enough" with respect to the Gaussian profile, i.e. we consider the signal integrated over the gaussian profile, until a maximum radius $R$ defined by the pinhole radius. We assume that the Gaussian beam is cylindrical : $w_1 = w_2 = w$ and we define $\eta^2$ the ratio between the pinhole section $S_{\mathrm{PH}} = \pi R^2$ and the section $S_{\mathrm{Gauss}} = \pi w^2$ of the image of the excitation volume in the pinhole plane. The effective beam section across the detection volume is therefore:

$$S_\eta = \int_{x^2+y^2<R_{\max}} f(x,y)dxdy = \int_0^{R_{\max}} \exp\left(-\frac{R^2}{w^2}\right) 2\pi R dR, \quad \text{with } R^2 = x^2+y^2 \tag{40}$$
$$= w^2\int_0^\eta e^{-r^2} 2\pi r dr, \quad \text{with } R/w = r, \quad dR = wdr \tag{41}$$
$$= \pi w^2[-e^{-r^2}]_0^\eta = \pi w^2\,(1-e^{-\eta^2}) \tag{42}$$

In the case of a weakly absorbing sample, we thus write:

$$F_\eta(t) = \frac{1}{S_\eta}\int_{x^2+y^2\le R^2} G(x,y,t)\; dxdy\;, \quad \text{with } G(x,y,t) \text{ as given by Eq. 28}$$
$$F_\eta(t) = \frac{1}{S_\eta}\exp(-kt)\int_{x^2+y^2\le R^2} \frac{\tilde{n}_0\, f(x,y)}{1+\tilde{n}_0\, h(t)\, f(x,y)}\; dxdy$$

$$F_\eta(t) = \frac{w^2}{S_\eta}\,\exp(-kt)\int_0^\eta \frac{\tilde{n}_0\, e^{-r^2}}{1+\tilde{n}_0\, h(t)\, e^{-r^2}}\, 2\pi r dr, \quad \text{with} \quad r^2 = \frac{x^2+y^2}{w^2}$$

$$F_\eta(t) = -\frac{1}{1-e^{-\eta^2}}\frac{\exp(-kt)}{h(t)}\int_{\tilde{n}_0 g}^{\tilde{n}_0 g\, e^{-\eta^2}} \frac{du}{1+u}, \quad \text{with} \quad u = \tilde{n}_0 h(t)\, e^{-r^2}, \quad du = -2r\, u dr$$

$$\boxed{F_\eta(t) = \frac{1}{1-e^{-\eta^2}}\frac{\exp(-kt)}{h(t)}\ln\left(\frac{1+\tilde{n}_0 h(t)}{1+\tilde{n}_0 h(t)\, e^{-\eta^2}}\right)} \tag{43}$$

We note that in the limit where $\eta$ goes to zero - i.e. the pinhole becomes "small enough" - we can write $e^{-\eta^2} = 1-\eta^2$, such that:

$$\ln\left(\frac{1+\tilde{n}_0 h(t)}{1+\tilde{n}_0 h(t)\, e^{-\eta^2}}\right) = \ln\left(\frac{1+\tilde{n}_0 h(t)}{1+\tilde{n}_0 h(t)\,(1-\eta^2)}\right) = \ln\left(\frac{1}{1-\frac{\tilde{n}_0 h(t)}{1+\tilde{n}_0 h(t)}\,\eta^2}\right) \simeq \frac{\tilde{n}_0 h(t)}{1+\tilde{n}_0 h(t)}\,\eta^2$$

$$\lim_{\eta\to 0} F_\eta(t) = \frac{\tilde{n}_0\, \exp(-kt)}{1+\tilde{n}_0 h(t)},$$

which is the expression obtained for a flat excitation profile (see Eq. 30). In all our experiments, we have $\eta^2 \leq 0.1$: the pinhole is small enough that the 'flat' approximation is very good.

## 2.7 Graphical illustrations

Throughout this subsection, we consider the case of a time-independent $\gamma$,
*i.e.* $h(\tau) = n_A^{-1}(1-\exp(-\tau))$, with $\tau = kt$, and $n_A = 2k/\gamma$.

### Effect of the spatial averaging on the apparent value of $\gamma$

Fig. S4 compares the decay kinetics expected according to $F_{\mathrm{PH}}(\tau)$ and $F_{\mathrm{noPH}}(\tau)$ defined as:

$$F_{\mathrm{PH}}(\tau) = \frac{\tilde{n}_0 \exp(-\tau)}{1+\tilde{n}_0 h(\tau)} \tag{44}$$

$$F_{\mathrm{noPH}}(\tau) = \frac{\exp(-\tau)}{h(\tau)}\ln(1+\tilde{n}_0 h(\tau)) \tag{45}$$

Here $F_{\mathrm{PH}}(\tau)$ is the decay kinetics as given by Eq. 3 and expected to occur with a flat excitation profile or a small enough pinhole (PH) in a confocal detection scheme. Conversely, $F_{\mathrm{noPH}}(\tau)$ is the decay kinetics as given by Eq. 39 and expected to occur if the fluorescence emission is averaged over the entire excitation volume, with a Gaussian energy profile (i.e. without pinhole, hence 'noPH' ).

When fitting decay kinetics obeying $F_{\mathrm{noPH}}(\tau)$ with $F_{\mathrm{PH}}(\tau)$ (dashed lines in Figure S4-right), even if the fit looks good at low initial exciton densities ($n(t=0) \leq n_A$), the $\gamma$ value is

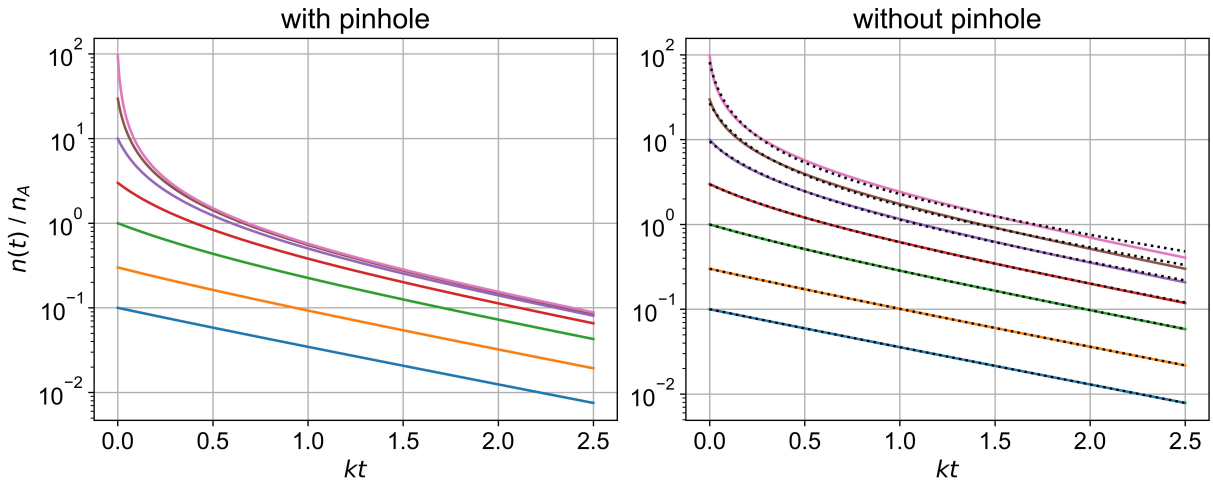


Figure S4: (See [1]) Comparison between $F_{\mathrm{PH}}(\tau)$ (left) and $F_{\mathrm{noPH}}(\tau)$ (right) for various initial exciton densities in units of $n_A$. The dashed lines in the right panel are the best fits of each individual decay curve $F_{\mathrm{noPH}}(\tau)$ when using $F_{\mathrm{PH}}(\tau)$ as the fitting function. No global fit seeking a $\gamma$ value common to all curves is possible here. The $\gamma$ values retrieved for each individual curve are underestimated by a factor of 2 at least, and further decrease when increasing the initial exciton density $n(t=0)$.

underestimated by a factor of at least 2, as can be understood by comparing the initial slopes, or Taylor expansions, of $F_{\mathrm{PH}}(\tau)$ and $F_{\mathrm{noPH}}(\tau)$ at early times (*i.e.* $\tau = kt \ll 1$):

$$F_{\mathrm{PH}}(\tau) \underset{\tau\to 0}{\simeq} \tilde{n}_0(1-\tau(1+\tilde{n}_0/n_A)) \tag{46}$$

$$F_{\mathrm{noPH}}(\tau) \underset{\tau\to 0}{\simeq} \tilde{n}_0\,(1-\tau(1+\tilde{n}_0/(2n_A))) \tag{47}$$

The fit becomes worse and worse when increasing the initial exciton density above $n_A$ with a $\gamma$ value apparently lower and lower, and underestimated by a factor of 2.6 when $n(t=0) = 10\,n_A$, or by a factor of 3.6 when $n(t=0) = 100\,n_A$.

**Effect of a deviation from the Gaussian profile**

Fig. S5 displays the results of the numerical integration of the Eq. 16 over the excitation volume with various pulse intensity profiles.

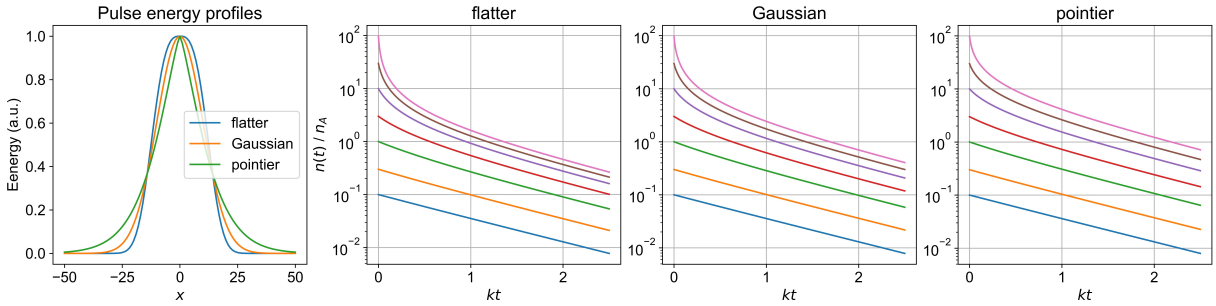


Figure S5: Comparison of the exciton decay kinetics as a function of initial exciton density at the pulse center (i.e. as a function of the pulse energy), for different pulse transverse profiles. When neglecting the effect of the integration over the excitation volume, and fitting such decay kinetics systematically with Eq 3, the apparent $\gamma$ value becomes lower when deviating further from the flat energy profile.

# 3 Time-resolved fluorescence acquisition and data processing

## 3.1 Experimental conditions

For time-resolved fluorescence data acquisition, the excitation beam is produced at 515 nm by a frequency-doubled Fiber Chirped Pulse Amplifier (Tangerine, Amplitude system) with a tunable repetition rate from 1 Hz to 2 MHz. The pulse duration is 300 fs and its spectral width is 2 nm FWHM. The experimental set-up is depicted in Figure 2 of the main paper. The excitation beam is propagated through a telescope (f=150mm, followed by f=200 mm) to adjust its diameter to 1.3 mm FWHM. It is then reflected by a dichroic filter (DF: Semrock Di02-R532-25x36) and focused in the circulated sample solution using a 10× microscope objective (Mo: Mitutoyo Plan Apo 10X, f=20 mm, NA=0.28, pupill diameter = 11.2 mm). The emitted fluorescence is collected through the same objective and is transmitted by the dichroic filter. A confocal detection scheme is implemented by placing a pinhole (PH) at the focal distance from two identical achromatic doublets (f=100mm, Thorlabs). The PH allows the selection of the fluorescence signal emitted from the central region of the excitation volume over which the excitation intensity is nearly spatially homogeneous. The spatially filtered and collimated fluorescence is propagated through a long pass filter (Thorlabs FGL530) to further attenuate residual excitation light, and focused by a camera objective (CO, Senko VFA5095H f=50 mm) into a spectrograph equipped with a streak camera (Hamamatsu streak scope C10627) operated in single photon counting mode. Thus, the measured fluorescence signal is spectrally and temporally resolved with 10ps time resolution.

A polarizer (P: Melles Griot Glan-Thompson prism) and an analyzer (A: Thorlabs WP25M-VIS) are used to set at magic angle (54.7°) the relative angle between the excitation and detection linear polarizations, thus cancelling the effects of fluorescence depolarization on the detected fluorescence intensity decay. The excitation power values were tuned utilizing a linear variable

neutral density. For higher excitation energies, the average power of the excitation beam was maintained low by down-scaling the laser pulse repetition rate. By doing so, we prevent the photodegradation of the sample eventually occurring after long experimental runs.

### 3.2 Measuring the laser spot section at the sample location

The excitation spot intensity profile is characterized by imaging the fluorescence spot - in the absence of the pinhole - using an auxiliary CCD camera imaging the plane of the sample. This must be done with very low excitation power, i.e. **in the absence of SSA**, in order to avoid saturation of the fluorescence intensity (hence broadening of the apparent fluorescence spot size). Indeed, only when the fluorescence intensity remains proportional to the excitation energy does the observed fluorescence intensity distribution precisely report on the excitation beam intensity distribution.

We carefully calibrated $\delta S = \delta_x^2$ the effective transverse surface element of the sample represented by each pixel. The calibration was done by imaging a reference, graduated target placed in the focal plane of the microscope objective (see Figure 2 in the main text), with no pinhole between both achromatic doublets. Then, for this calibration to be reliable, we have to make sure that the sample (the water solution inside a flow cell of thickness 0.2 to 0.5 mm) is placed in the same plane. To do so, we mounted the cuvette holder on a manual translation stage and noticed that we could precisely detect the positions where the successive glass/air and glass/water interfaces of the flow cell are in the objective focal plane, by imaging the pump beam reflections on these interfaces. Finally, we move the translation stage to the middle position between both water/glass interfaces.

Fig. S6 shows an example of images recorded with the auxiliary CCD camera. In the absence of pinhole, the transverse profile of the excitation volume is relatively well fitted by a 2-dimensional Gaussian function.

We define $P(i,j)$ the digitized signal on each pixel of the camera. We assume that $P(i,j)$ is proportional to the sum along the $z$ axis of the number $n(x = i\delta_x, y = j\delta_x, z)\delta S dz$ of photons emitted from each elementary volume $\delta S dz$. More precisely, we write (with $C$ a constant of proportionality):

$$
\begin{aligned}
P(i,j)\,\delta S &= C \int_0^l n(x = i\delta_x, y = j\delta_x, z) dz\, \delta S \\
P(i,j) &= C\; l\; \tilde{n}(x = i\delta_x, y = j\delta_x) \\
P(i,j) &= C\; l\; \tilde{n}_0\; f(x = i\delta_x, y = j\delta_x) \quad \text{(from Eq. 15 and Eq. 24)} \\
\Rightarrow \quad \max(P(i,j)) &= C\; l\; \tilde{n}_0 \max(f(x = i\delta_x, y = j\delta_x)) \;=\; C\; l\; \tilde{n}_0\, f(0,0) \;=\; C\; l\; \tilde{n}_0
\end{aligned}
$$

We therefore can write:

$$
\frac{P(i,j)}{\max(P(i,j))} \;=\; p(i,j) \;=\; f(x = i\delta_x, y = j\delta_x) \tag{48}
$$

$$
\Rightarrow \quad S \;=\; \sum p(i,j)\delta S \tag{49}
$$

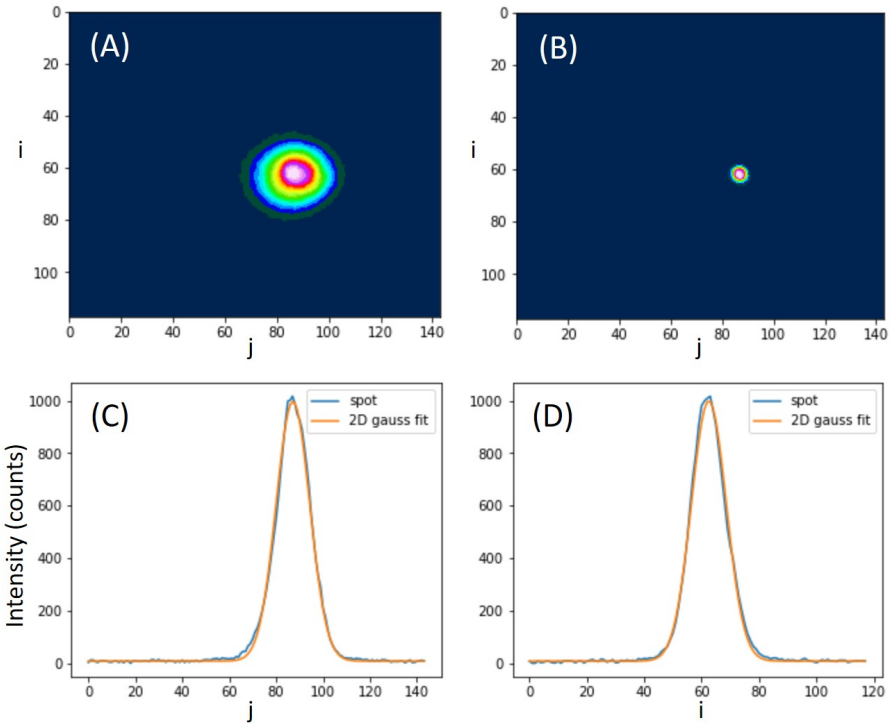


Figure S6: Image of the sample plane in the absence (A) and presence (B) of the pinhole of diameter 50 $\mu$m in the conjugated, pinhole plane. In the absence of pinhole (A), the excitation transverse profile is well fitted by a 2-dimensional Gaussian functions as illustrated by the profiles along $j$ (raws, panel C) and $i$ (lines, panel D).

Hence we analyze the fluorescence spot images $P(i,j)$ as indicated by Eq. 48 and Eq. 49 in order to determine the laser spot section $S$ in micrometers. This quantity is essential for a careful calibration of the fluorescence intensity in terms of exciton density as we will discuss in section 3.5 below. As an example, we find $S$=298 pixels for Figure S6A. The analysis of the CCD image of the 50 $\mu$m pinhole reveals a section $S_{\rm PH}$=16.8 effective pixels, corresponding to a ratio $\eta^2 = S_{\rm PH}/S_{\rm Gauss} \simeq 1/18$ (see subsection 2.6). In all experiments reported here, we use a 25 $\mu$m pinhole, while typical spot sections are in the range of 300 $\mu$m$^2$ to 1500 $\mu$m$^2$ on the sample (i.e. $\sim$ 60 to 300 pixels in the CCD image of the pinhole plane), corresponding to a Rayleigh length $L = S/\lambda$ of 0.6 mm or more ($\lambda = 0.515$ $\mu$m). This is longer than the sample thickness of 0.2 or 0.5 mm, defined by the two types of flow cells used in the various experiments.

### 3.3 Testing the linear regime of rhodamine dye excitation

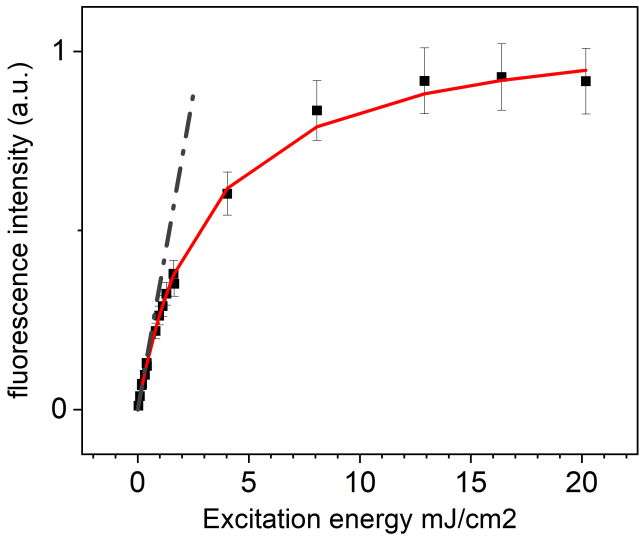


Figure S7: Fluorescence intensity (a.u.) of a water solution of rhodamin B at concentration 3 mM as a function of excitation intensity, detected in the confocal configuration in the presence of the pinhole. The individual chromophore absorption starts deviating from the linear regime at excitation intensity exceeding 1mJ/cm$^2$, never reached in the TR fluorescence experiments with the SC, nor in the transient absorption experiments (see below).

### 3.4 Data acquisition and processing

The spectrally and temporally resolved fluorescence signal is successively recorded over two (or three) streaking time windows of 1 ns, 5 ns (and/or 20 ns). The temporal response function of the streak camera is a Gaussian of $\approx$ 10ps standard deviation for 1 ns time window. For each time window, the measured signal is baseline corrected and spectrally integrated over the full fluorescence emission spectral range. Thereafter, for each given excitation power, a complete fluorescence decay kinetics is reconstructed by appending the individual decays corresponding to each detection time window. Figure S8-A illustrates the full fluorescence signal decay over 20 ns for 30w% dye-loaded ONPs reconstructed by scaling the relative amplitudes of the spectrally-integrated curves recorded over the three streaking time windows. We note that global analysis/fitting models were performed on the exciton population kinetics obtained from such reconstructed fluorescence decay kinetics. This approach has two advantages. First and foremost, it allows resolving the decay at early times with the best permissible resolution in the 1 ns time window. Secondly, owing to the single-photon counting operation, the fluorescence tail can be detected with a high signal-to-noise ratio in the 20 ns time window.

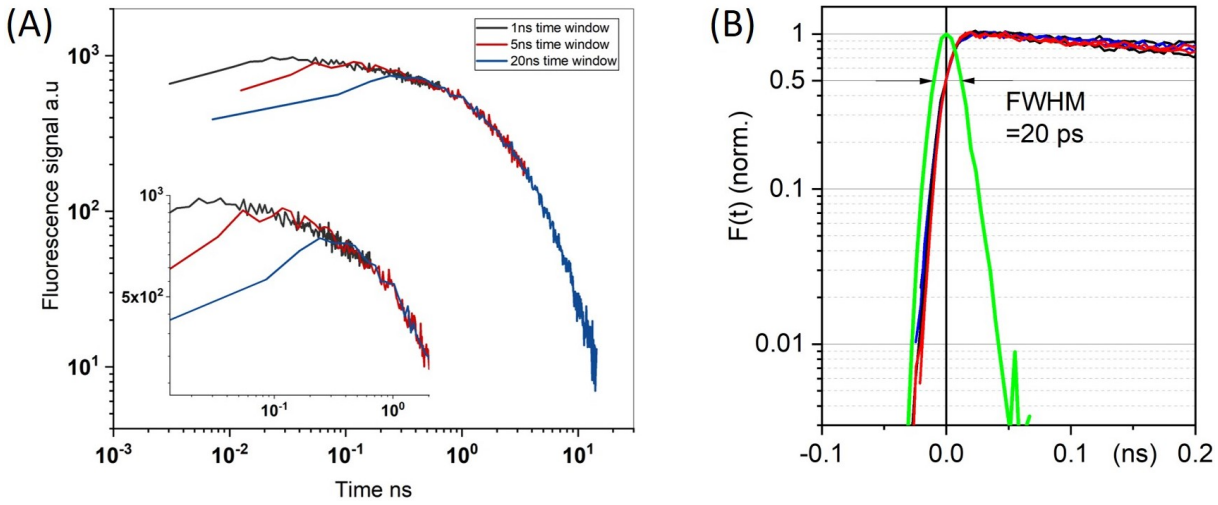


Figure S8: (A) Reconstruction of the fluorescence decay kinetics measured for 30w % dye-loaded ONP utilizing the streak camera setup. The inset highlights the decay up to 1ns. The fluorescence intensities are measured over 1 ns, 5 ns and 20 ns streaking time windows. A scaling factor is computed to ensure optimal overlapping. (B) Zoom on the early times of Figure 3B of the main text, together with the streak camera response function (green) on the 1 ns streaking time window, recorded by monitoring a reflection of the 300-fs excitation pulse.

The fluorescence decay kinetics (measured on three time windows and reconstructed as explained above) are recorded with a given excitation laser power $P$ in $\mu$W and repetition rate $r$ in kHz. We also calibrate that, at the location of the sample the laser power is $f = 0.86$ times the power that we measure at a different, more accessible location along the excitation laser beam path. The sample is thus excited with and energy per pulse:

$$\mathcal{E}_0 = \frac{f \times P}{r}, \quad \text{in nJ.} \tag{50}$$

We excite the samples with minimum laser repetition rate to avoid sample photodegradation. We therefore record the fluorescence signal with no attenuation filter in front of the spectrograph entrance slit, and a fixed widely opened slit. We operate the streak camera in photon counting mode, with the SC-CCD exposure time fixed at 100 ms, and 2 to 4% photon detection probability per pixel at maximum. One acquisition consists of accumulating a fixed number of 2500 SC-CCD frames, taking a bit more that 250 s (the SC-CCD readout rate is close to 10 frames per second). When reducing the energy per excitation pulse in order to test the linear regime of excitation (i.e. no SSA) we operate at maximum repetition rate $r = 200$ kHz, and may even increase the SC-CCD exposure time $T_x$ to a value longer than the usual 100ms in order to maintain the photon detection probability per SC-CCD frame in the same range. Conversely, when increasing the energy per pulse to observe large SSA rates, we reduce the repetition rate $r$

(down to 100 Hz at minimum), so as to maintain a comparable average light power and therefore a comparable photon counting rate. Eventually, to account for these variations in acquisition conditions, we rescale the raw streak camera signals $s(t)$ to produce fluorescence decay curves $\tilde{s}(t)$ that can be quantitatively compared to one another, according to:

$$\tilde{s}(t) = \frac{s(t)}{r \times T_x} \tag{51}$$

### 3.5 Signal absolute calibration in units of exciton density in the ONP's.

The signal $\tilde{s}(t)$ is directly proportional to the total fluorescence signal $F(t)$ emitted in the detection volume, as defined by Eq. 16. More precisely, provided the signal amplitude is not limited by the experimental time resolution, i.e. at excitation powers where SSA does not lead to an ultrafast exciton decay, the maximum of the signal $\tilde{s}(t)$ is proportional to $F(t=0) = \tilde{n}_0$ according to Eq. 46 or Eq. 47.

From the measurement of the excitation beam energy $\mathcal{E}_0$ ( Eq. 50) and section $S$ at the sample location (see subsection 3.2), we infer the R18 dye excitation probability $\mu(\vec{r} = \vec{0})$ at the laser pulse center and at the entrance of the sample (see Eq 13):

$$\mu(x = y = z = 0) = \frac{\varepsilon \ln(10)}{N_A\, h\nu} \frac{\mathcal{E}_0}{S}, \tag{52}$$

where $\varepsilon = 35000$ /M/cm $= 4.7 \times 10^7$ cm$^2$/mol is the extinction coefficient of R18 in the ONP **at the excitation wavelength** of 515 nm, and $h\nu = 3.86 \times 10^{-19}$ J is the excitation photon energy. Hence we get:

$$\frac{\varepsilon \ln(10)}{N_A\, h\nu} = 0.347 \text{ cm}^2/\text{mJ}.$$

In other words, with a pulse energy density $\dfrac{\mathcal{E}_0}{S} = 0.1$ mJ/cm$^2$, the dye excitation probability is 3.47% at the laser pulse center and at the entrance of the sample.

Then, knowing the dye number density $\rho$ in the ONPs, and the sample absorbance $A$ in the flow cell (flow cell thickness = 0.2 or 0.5 mm depending on the flow cell used in each experiment), we infer the $z$-averaged peak exciton density $\tilde{n}_0$, according to:

$$\boxed{\tilde{n}_0 = \rho \times \frac{\varepsilon \ln(10)}{N_A\, h\nu} \frac{\mathcal{E}_0}{S} \times \frac{1 - 10^{-A}}{A \ln(10)}}, \tag{53}$$

Fig. S9 illustrates how Eq. 53 is used to calibrate the measured decay kinetics in units of exciton density. The absolute calibration relies on the knowledge of the dye number density $\rho$ in the ONP's, which is evaluated as follows. By definition, we can write:

$$\rho = \frac{m_{dye}}{M_{dye} \times V_{ONP}} \times N_A,$$

where:

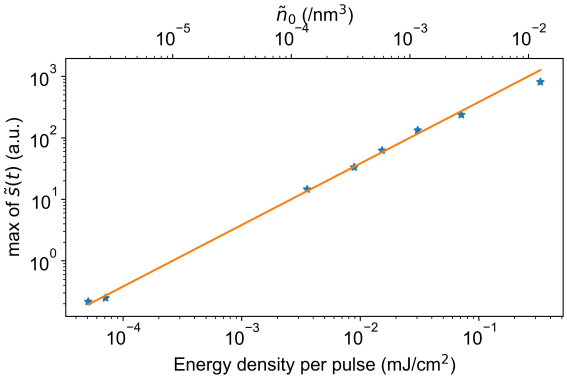


Figure S9: Example of calibration of decay kinetic signals (in arbitrary units) in units of exciton density (in nm$^{-3}$) for 30 wt%-loaded nanoparticles. Blue stars represent the maximum signal $\tilde{s}(t=0)$ (in arbitrary units) recorded as a function of the excitation energy density. Eq. 53 is used to convert the excitation pulse energy density (in mJ/cm$^2$) into peak exciton density (in nm$^{-3}$). The slope of the orange line (in nm$^3$), defines the calibration factor to rescale the signal $\tilde{s}(t)$ in exciton density.

- $m_{dye} = \delta \times m_{poly}$ is the total mass of dyes (ions + counterions) expressed as a function of the total mass of polymer $m_{poly}$ and $\delta$ the dye loading in w% of polymer,
- $M_{dye} = 1375.11$ g/mol is the molar mass of dyes (ions + counterions),
- $V_{ONP}$ is the total volume of all ONP's in solution expressed as a function of the average polymer (and dye) density $d$=1g/cm$^3$:

$$V_{ONP} = \frac{m_{poly} + m_{dye}}{d} = (1+\delta)\frac{m_{poly}}{d}.$$

Hence:

$$\rho = \frac{\delta}{1+\delta} \times \frac{d\,N_A}{M_{dye}} = \frac{\delta}{1+\delta} \times 4.38 \times 10^{20}\ \text{cm}^{-3} \tag{54}$$

$$\boxed{\rho = \frac{\delta}{1+\delta} \times 0.438\ \text{nm}^{-3}} \tag{55}$$

We have been investigating ONPs with dye loading $\delta = 30\%$ or $100\%$, corresponding to dye number densities as large as $\rho = 0.10$ or $0.22$ dye per nm$^3$.

# 4 Complementary time-resolved fluorescence data

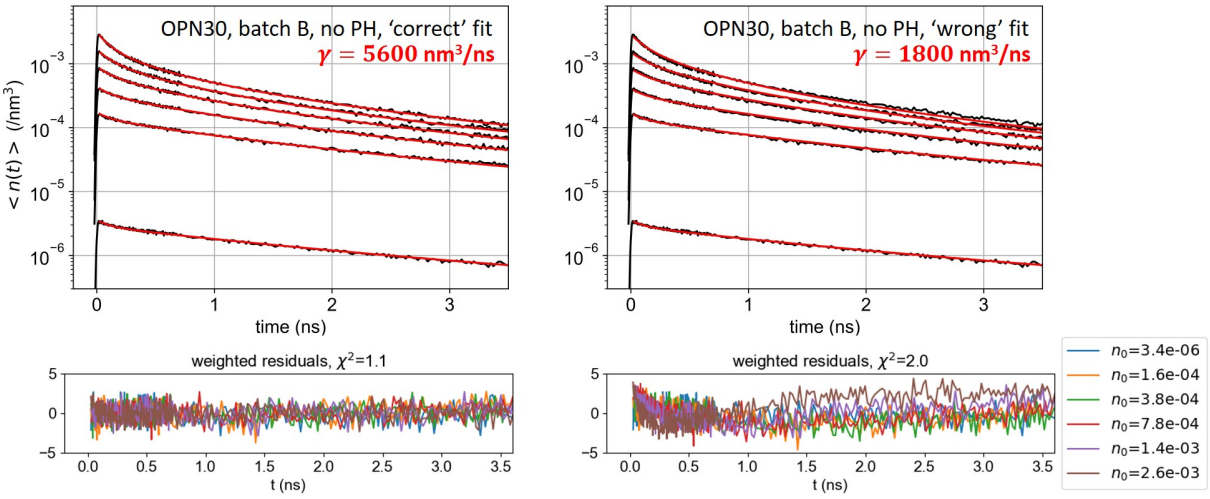


Figure S10: (See [1]) ONP30, batch B: Exciton density (in $\mathrm{nm}^{-3}$) decay kinetics averaged over the detection volume without any pinhole (black lines), for increasing excitation powers. The red lines are the result of the global fit of the decay kinetics with $K_{\mathrm{noPH}}(t)$ yielding $\gamma$ =5600 $\mathrm{nm}^3$/ns (left), or with $K_{\mathrm{PH}}(t)$ yielding $\gamma$ =1800 $\mathrm{nm}^3$/ns (right). In the right panels, the model is not good at fitting the asymptotes which do not merge when increasing power. What is more, the resulting $\gamma$ value is underestimated by a factor of 3. The individual fit of each decay kinetics with $K_{\mathrm{PH}}(t)$ appears good (not shown) but erroneously results in a $\gamma$ value reducing with increasing excitation power. Only when using the appropriate fitting function $K_{\mathrm{noPH}}(t)$ (left panels) do we obtain a satisfying global fit, with a unique $\gamma$ value.

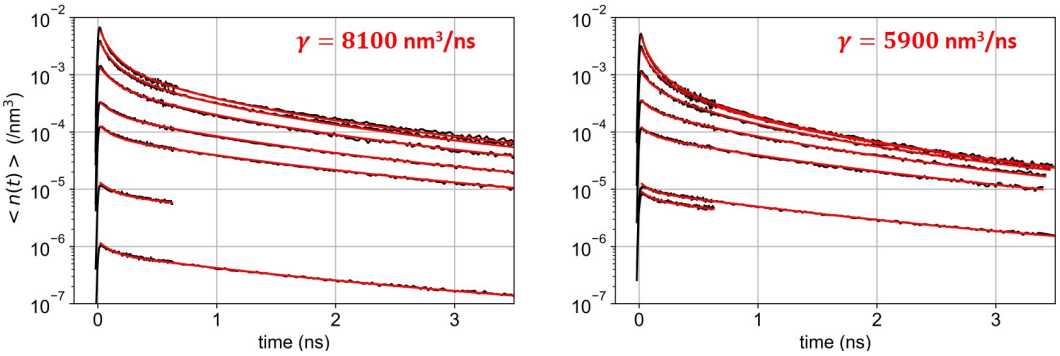


Figure S11: ONP100, batch A: Exciton density (in $\mathrm{nm}^{-3}$) decay kinetics averaged over the detection volume without any pinhole (left) and with pinhole (right), for increasing excitation powers.The red lines are the result of the global fit of the decay kinetics with $K_{\mathrm{noPH}}(t)$ yielding $\gamma$ =8100 $\mathrm{nm}^3$/ns (left), or with $K_{\mathrm{PH}}(t)$ yielding $\gamma$ =5900 $\mathrm{nm}^3$/ns (right). Both panels display the results of distinct experimental campaigns, performed in different conditions (with or without pinhole) and fitted with the appropriate functions: the difference between both $\gamma$ values, *i.e.* $\pm$ 1100 $\mathrm{nm}^3$/ns, should be assigned here to the typical uncertainty characterizing the overall repeatability of the measurements.

## 5 Modeling the light-induced formation of a quencher species

Here we compare two models, 'Q2' and 'Q1', where the quencher photoproduction would occur from the doubly-excited $S_p$ state produced by SSA, or directly from the singly-excited $S_1$ state produced by light absorption, respectively:

- Model 'Q2' (used in the main text):

$$\begin{aligned} \frac{dn(t)}{dt} &= -(k+\gamma_Q n_Q(t))n(t) - (1+\beta)\frac{\gamma(t)}{2}n^2(t) + n_0 P(t) \\ \frac{dn_Q(t)}{dt} &= \frac{\beta}{2}\gamma(t)\, n^2(t) \end{aligned} \tag{56}$$

- Model 'Q1':

$$\begin{aligned} \frac{dn(t)}{dt} &= -(k+k_Q+\gamma_Q n_Q(t))n(t) - \frac{\gamma(t)}{2}n^2(t) + n_0 P(t) \\ \frac{dn_Q(t)}{dt} &= k_Q\, n(t) \end{aligned} \tag{57}$$

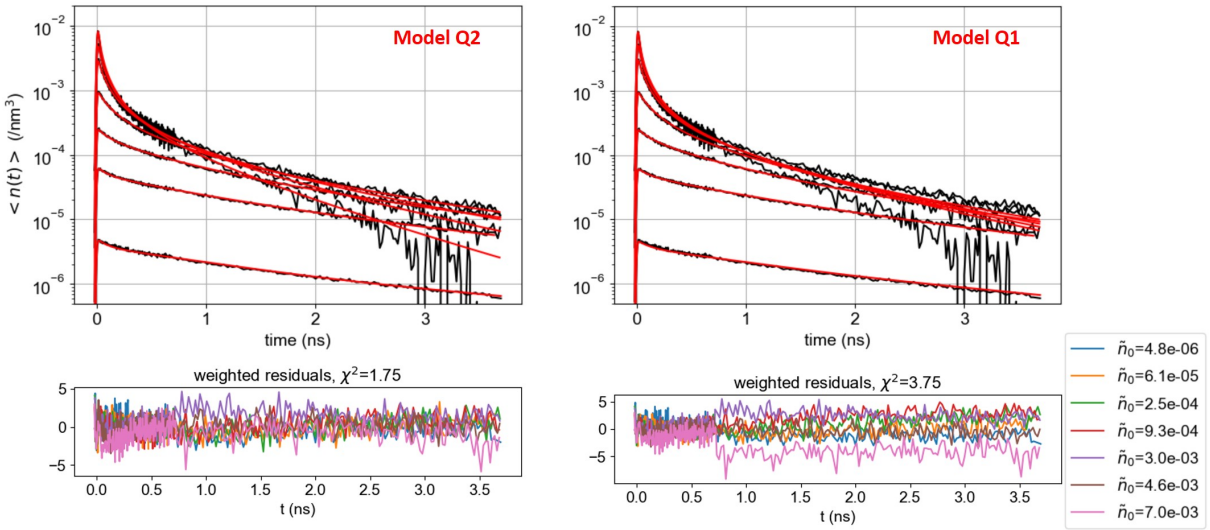


Figure S12: (See [1]) ONP100, batch B: Exciton density (in $\mathrm{nm}^{-3}$) decay kinetics detected with a pinhole (black lines), for increasing excitation powers. These are the same data as in Figure 4C in the main text. The red lines are the result of the global fit with model 'Q2' (left) or 'Q1' (right). While model 'Q2' reproduces the sudden decrease of the exciton lifetime when $\tilde{n}_0$ exceeds $10^{-3}$ $/\mathrm{nm}^3$ (left), model 'Q1' predicts a more gradual variation of the exciton lifetime as a function of excitation power, which does not fit so well the observation (right). Note that the sudden increase in the residuals at $t \simeq 0.7$ns (bottom panels) is due to the sudden reduction of the noise amplitude (used to weight the residuals) for data recorded on longer time windows (see the streak camera data appending procedure illustrated in Figure S8-A).

## 6 Förster radius $R_0$ for homo-FRET

Incoherent exciton hopping from dye to dye is described as a resonant energy transfer from an R18 dye in its excited state ($S_1$, the donor D) to a nearby R18 dye in its ground state ($S_0$, the acceptor A). This process is sometimes called homo-FRET. The corresponding Förster radius $R_0$ - i.e. the distance at which the energy transfer quantum yield is 50% - is given by: [7]

$$R_0 = 0.2108 \left[ \kappa^2 \phi_D n^{-4} \int_0^\infty I_D(\lambda) \varepsilon_A(\lambda) \lambda^4 \, d\lambda \right]^{1/6}, \tag{58}$$

with $\kappa^2$ the orientational factor, $\phi_D$ the donor fluorescence quantum yield in the absence of any energy acceptor, and $n$ is the refractive index of the medium. The integral expresses the spectral overlap between the donor's fluorescence spectrum $I_D(\lambda)$ normalized such as $\int_0^\infty I_D(\lambda)\, d\lambda = 1$, and the acceptor's absorption $\varepsilon_A(\lambda)$ in units of $\mathrm{M}^{-1}$ $\mathrm{cm}^{-1}$. In the present case of homo-FRET, $\varepsilon_A(\lambda) = \varepsilon_D(\lambda)$ is the R18 dye extinction coefficient.

We compute the spectral overlap from the steady state fluorescence and absorption spectra presented in Figure 3A of the main text, after scaling the absorption spectrum according to $\varepsilon_D(\lambda = \lambda_{max}) = 125000\ \mathrm{M}^{-1}\ \mathrm{cm}^{-1}$.[8] In the absence of homo-FRET and any quenching species, the fluorescence quantum yield is $\phi_D = 0.99$, measured on ONPs with a low dye-loading of 0.1w%. [9] The PMMA refractive index is $n = 1.49$.[10] Since the dyes are randomly distributed within the rigid polymer solution in the ONPs, the orientational factor is $\kappa^2 = 0.476$.[7]

Applying these parameters to Eq.58, we find $R_0 = 5.27$ nm and $R_0 = 5.21$ nm for 30 wt% and 100 wt% dye-loaded ONPs, respectively.

# 7 Transient absorption spectroscopy and Förster radius for EEA

A chirped-pulse, Ti:Sa, regenerative amplifier (Amplitude) is used to pump a commercial optical parametric amplifier (TOPAS, Light Conversion) with an 800nm, 40-fs pulse at 5 kHz repetition rate. The TOPAS is tuned and its output pulse frequency-doubled so as to produce a $\simeq 60$ fs pump pulse at 515 nm. A white light supercontinuum is generated by focusing about 2 $\mu$W of the fundamental 800-nm pulse in a $CaF_2$ crystal and used as the probe pulse. The pump and probe are focused to $\simeq 70\mu$m and $\sim 35\mu$m, respectively, and overlapped. A water solution of 30 %w dye-loaded ONPs is circulated in a 0.5 mm thick fused silica cuvette placed at the location of the pump and probe spatial overlap. The sample absorbance is $\simeq 0.04$ at the pump wavelength. Pump and probe are linearly polarized with magic angle (54°) relative orientation.

While the SC and its single photon counting capability enables recording fluorescence decay kinetics with extremely low excitation powers, higher excitation probabilities are required to detect a decent signal in the TAS set-up with the ONP samples. Three pump-probe experiments were carried out with three different pump pulse energies of 5 nJ, 10 nJ and 24 nJ, corresponding to rhodamine dye excitation probabilities of approximately 3.1, 6.2 and 14 %, respectively. At these excitation probabilities, the exciton decay kinetics is dominated by SSA.

We perform a multiexponential, global fit of the TAS data: three resolved time constants (i.e. larger than the TA time resolution of 60 to 70 fs) are sufficient to minimize the reduced $\chi^2$ in these fits. The corresponding Decay-Associated Spectra (DAS) are displayed in Figure S13. While the time constants extracted from these multiexponential fits have no immediate physical meaning (indeed the expected decay kinetics is not multiexponential but obeys Eq. 30), the DAS reveal the time evolution of the spectroscopic signature of the excitons in the ONP's. The shortest of these time constants is in the range of 0.7 to 1.2 ps depending on the excitation probabilities. The corresponding DAS reveal spectral relaxation associated to vibrational relaxation in $S_1$, as also observed in rhodamine B in water solution (not shown) on a very similar time scale. Exciton population decay and GSB recovery may also occur already on the ps time scale, especially in the 24-nJ-pump data. Noticeably, the DAS corresponding to intermediate time scales of 20 to 60 ps are identical in all three experiments and reproducibly different (the negative band is narrower - likely the signature of vibrationally hot $S_1$ or $S_0$ states) from the DAS characterizing the longest time constants in the range 300 to 700 ps. The latter are also identical in all three experiments and we compute their average, that we name $\mathrm{DAS}_{long}$ in the following.

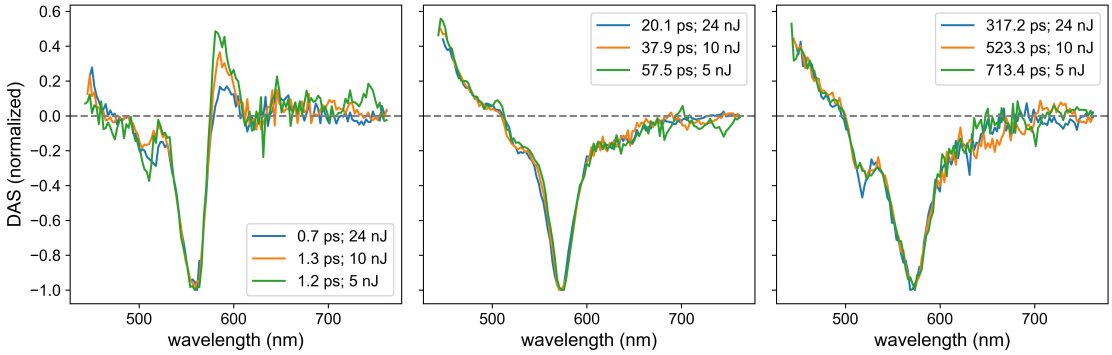


Figure S13: Result of the global analysis of the TA data recorded on ONP30 with pump pulse energies of of 5 nJ, 10 nJ and 24 nJ: The Decay-Associated Spectra (DAS) corresponding to (left) the fast, (middle) intermediate and (right) slowest time constants are normalized and compared among the three experiments.

The transient absorption signal revealed by $\mathrm{DAS}_{long}$ is the superposition of three contributions which are ground state bleach (GSB), stimulated emission (SE) and excited state absorption (ESA). Subtracting the GSB and SE contributions allows us to retrieve the ESA spectrum from this $\mathrm{DAS}_{long}$. While the GSB is directly proportional to the opposite of the absorption spectrum $\varepsilon_{GS}(\lambda)$, the (negative) extinction coefficient for stimulated emission $\varepsilon_{SE}(\lambda)$ can be inferred from the fluorescence spectrum $A(\lambda)$. Indeed, following the reasoning by Strickler & Berg [11] (see also ref. [12]) we shall first note that the Einstein relation between spontaneous and stimulated emission allows us to write: $\varepsilon_{SE}(\nu) \propto A(\nu) \times \nu^2$ where the spectra are expressed as a function of the photon frequency $\nu$. When writing the spectra as a function of wavelength, this relation becomes $\varepsilon_{SE}(\lambda) \propto A(\lambda)\lambda^4$ (See e.g. ref. [7] about the conversion from wavelength to frequency axis for emission spectra). Then, the intensities of stimulated emission and absorption spectra are related to one another because both extinction coefficients describe light-molecule interaction involving the same transition dipole moment, such that (see [11]) :

$$\int \frac{\varepsilon_{SE}(\lambda)}{\lambda} d\lambda = -\int \frac{\varepsilon_{GS}(\lambda)}{\lambda} d\lambda.$$

Eventually we compute the SE extinction coefficient (in units of /M/cm) as follows:

$$\varepsilon_{SE}(\lambda) \quad = \quad -\frac{\int \frac{\varepsilon_{GS}(\lambda)}{\lambda} d\lambda}{\int A(\lambda)\lambda^3 d\lambda} \, A(\lambda)\lambda^4 \tag{59}$$

Figure S14-A illustrates the spectral shape expected for the sum of GSB and SE, as inferred from the ground state absorption and the fluorescence spectrum (Eq. 59). This contribution must be subtracted to $\mathrm{DAS}_{long}$ in order to recover the ESA extinction coefficient $\varepsilon_{ESA}(\lambda)$. Figure S14-B and S14-C present two different, plausible "scalings" of the SE + GSB contribution in order to

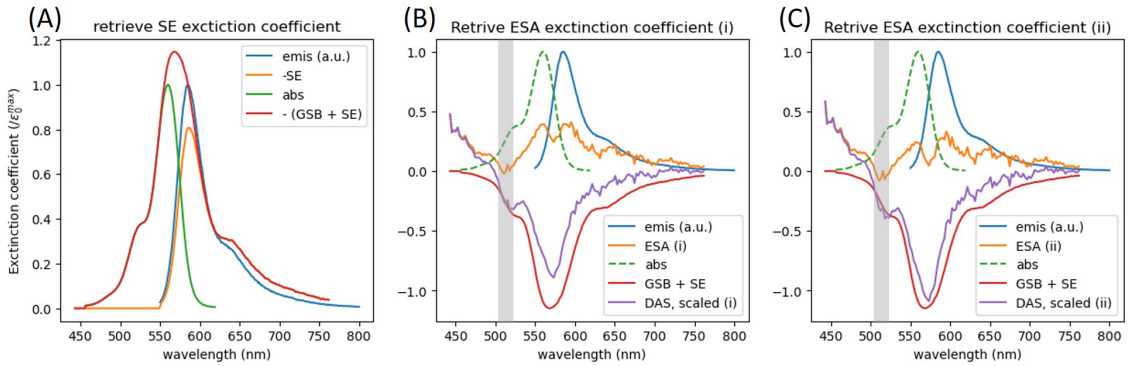


Figure S14: (A) Construction of the expected GSB and SE spectral shapes from the steady-state absorption and emission spectra (see Eq. 59), respectively. The red line is the opposite of the sum GSB+SE. (B) and (C) Evaluation of the ESA extinction coefficient (orange lines) computed as the difference between the scaled $\mathrm{DAS}_{long}$ and the expected GSB+SE contribution, with two plausible "scalings" (i) and (ii) of the GSB+SE contribution. The overlap between the retrieved ESA spectra and the emission spectrum (blue line) defines the Förster radius $R_{EEA}$ for energy transfer between two chromophores in their excited states.

evaluate the error bar on the retrieved ESA intensity. In the end, we are interested in computing the overlap of this ESA spectrum with the exciton emission spectrum. Using both evaluations of the ESA spectrum we infer the ratio between $R_{EEA}$ the Förster radius characterizing the energy transfer between two chromophores in their excited states hence EEA: $R_{EEA} = (1.10 \pm 0.05) \times R_0$, with $R_0$ characterizing the homo-FRET responsible for exciton hoping.

## 8 Pulsed versus cw illumination

By definition of the absorption cross section $\sigma$ (in $\mathrm{cm}^2$), and within the linear regime of excitation (i.e. $\sigma$ independent from the excitation light intensity), the rate $k_{abs}(t)$ of photon absorption by the population of dyes in their ground state $n_{GS}(t)$, is given by

$$k_{abs}(t) = \sigma I(t)/(h\nu), \tag{60}$$

where $I(t)$ is the (time-dependent) incident light intensity, $h\nu$ the photon energy - hence $I(t)/(h\nu)$ is the incident photon flux. We note here, that $\sigma$ is conceptually the same physical quantity as the extinction coefficient $\varepsilon$ but written in different units: $\sigma = \varepsilon \ln 10/N_A$.[7]

In the following, we will assume a low enough excitation probability, such that the dye ground state population $\rho$ (see Equation 55 for the evaluation of $\rho$) is weakly depleted and can be assumed to remain constant. In a CW experiment, this is practically always a very good approximation. In a pulsed experiment, this means, that we remain in the linear regime of excitation, i.e. with an energy density typically lower than 1 $\mathrm{mJ/cm}^2$, according to Figure S7.

We now rewrite Equation 1 in a more general form including the source term accounting for the rise of the exciton population $n(t)$ upon light absorption by the ground state population $\rho$ with rate $k_{abs}(t)$ :

$$\frac{dn(t)}{dt} = +k_{abs}(t)\rho - kn(t) - \frac{1}{2}\gamma(t)n^2(t), \tag{61}$$

**Pulsed excitation.** Provided the pulse duration is much faster than the excited state population kinetics, we can model a pulsed experiment without the source term (i.e. Equation 1), but define the initial condition:

$$n(t=0) = \int_{-\epsilon}^{+\epsilon} k_{abs}(t)\rho dt = \rho\frac{\sigma}{h\nu}\int_{-\epsilon}^{+\epsilon} I(t)dt = \rho\frac{\sigma}{h\nu}\frac{\mathcal{E}_0}{S}$$

where $\epsilon$ is a time interval short compared to the excited state dynamics, and long compared to the pulse duration, $\mathcal{E}_0/S$ is the pulse energy density in J/cm$^2$. We may thus define the excitation probability per pulse as being:

$$\eta = \frac{n(t=0)}{\rho} = \frac{\sigma}{h\nu}\frac{\mathcal{E}_0}{S} = \frac{\varepsilon\ln(10)}{N_A\, h\nu}\frac{\mathcal{E}_0}{S}, \tag{62}$$

which is the expression already given in Equation 15.

We observe (see main text) that EEA becomes significant with excitation probabilities approaching $\eta_A = 0.1\%$, which is thus achieved for pulse energy densities as low as:

$$\mathcal{E}_A/S = \eta_A\frac{h\nu}{\sigma}$$

With an excitation wavelength of 515nm - i.e. $h\nu = 3.86\times10^{-19}$ J - the extinction coefficient of R18 in ONPs is $\varepsilon = 35000$ /M/cm, such that $\sigma = 1.34\times10^{-16}$ cm$^2$. Hence EEA becomes significant when the pulse energy density approaches $\mathcal{E}_A/S = 2.9$ $\mu$J/cm$^2$. In the present time-resolved photoluminescence experiment, we use a 300 fs pulse such that the corresponding pulse peak intensity is as large as $\simeq 10^7$ W/cm$^2$. This is a huge peak intensity, but the pulse duration is so short that it indeed corresponds to a low (0.1%) excitation probability per pulse.

**Continuous wave (cw) excitation.** With cw light, i.e. time-independent $k_{abs}$, the exciton population in the stationary regime $n_{cw}$ is given by:

$$\frac{dn}{dt} = 0 = \rho k_{abs} - \frac{n_{cw}}{\langle\tau\rangle} - \frac{1}{2}\gamma n_{cw}^2 \tag{63}$$

$$0 = -n_A\rho\langle\tau\rangle k_{abs} + n_A n_{cw} + n_{cw}^2 \tag{64}$$

$$i.e.\quad n_{cw} = \frac{n_A}{2}(\sqrt{1+4\langle\tau\rangle k_{abs}\rho/n_A} - 1) \tag{65}$$

Here for simplicity, we introduce the average lifetime $\langle\tau\rangle$, rather than considering a distribution of lifetimes (see Table 1 in the main text), and accordingly, we define $n_A = 2/(\gamma\langle\tau\rangle)$, assuming that $\gamma(t) = \gamma$ is constant.

Excitons decay either "naturally" with rate $1/\langle\tau\rangle$ or via EEA with rate $\gamma n_{cw}/2$. Hence the fluorescence quantum yield $\phi$ is given by:

$$\phi = \frac{k_{rad}}{1/\langle\tau\rangle + \gamma n_{cw}/2} = k_{rad}\langle\tau\rangle \frac{1}{1 + n_{cw}/n_A} \tag{66}$$

$$\phi = \phi_0 \ \frac{1}{1 + n_{cw}/n_A}, \tag{67}$$

where $\phi_0 = k_{rad}\langle\tau\rangle$ is the fluorescence quantum yield at low excitation intensity (i.e. no EEA). For instance $\phi_0 = 0.44$ for ONP30, see Table 1 in the main text.

The EEA decay mechanism becomes significant - i.e. reduces notably the fluorescence quantum yield - when $n_w$ approaches $n_A$. This corresponds to absorption rates approaching $k^A_{abs}$ given by:

$$4\langle\tau\rangle k^A_{abs}\rho/n_A = 8$$
$$i.e. \quad k^A_{abs} = \frac{2n_A}{\rho\langle\tau\rangle} = \frac{4}{\rho\gamma\langle\tau\rangle^2}$$

According to Equation 60, the corresponding cw light intensity would be:

$$I_A = k^A_{abs}\frac{h\nu}{\sigma} = \frac{4}{\rho\gamma\langle\tau\rangle^2}\frac{h\nu}{\sigma} = 3.7 \text{ kW/cm}^2,$$

where we take $\langle\tau\rangle = 2.35$ ns as in the case of ONP30.

By contrast, no more than few W/cm$^2$ cw light intensity is used for single ONP fluorescence detection. In this regime, $n_{cw} \ll n_A$ and we can even write $4\langle\tau\rangle k^A_{abs}\rho/n_A \ll 1$ to Taylor expand Equation 65, such that:

$$n_{cw} = \rho k_{abs}\langle\tau\rangle$$

With 1 W/cm$^2$ cw light intensity at 532 nm [13] - where $\varepsilon = 47000$ /M/cm, i.e. $\sigma = 1.8 \times 10^{-16}$ cm$^2$ - the photon absorption rate of the R18 dye is $k_{abs} \simeq 500$ s$^{-1}$, corresponding to an average excitation probability of $n_{cw}/\rho = k_{abs}\langle\tau\rangle$ of order $10^{-6}$. With $\rho V \simeq 4000$ dyes per ONP, each ONP absorbs $\sim 2 \times 10^6$ photons per second, but the average number of exciton per ONP in the photostationary state remains of order $n_{cw} \times V = 4000 \times k_{abs}\langle\tau\rangle \simeq 0.005$.

Assuming Poisson statistics with average value 0.005, the probability to find 2 excitons in an ONP is $\simeq 0.005^2/2 \simeq 12 \times 10^{-6}$. In the same way as we wrote the probability $\phi$ that an exciton decays radiatively (Equation 67), we can write the probability $p_{EEA}$ that an exciton decays via EEA - provided there are (at least) 2 excitons in the ONP, i.e. $n \geq 2/V$:

$$p_{EEA} = \frac{\gamma n/2}{1/\langle\tau\rangle + \gamma n/2} = \frac{n/n_A}{1 + n/n_A} \tag{68}$$

$$\text{with } n = \frac{2}{V} \quad \Rightarrow \quad p_{EEA} = \frac{2}{2 + Vn_A} \simeq \frac{1}{3} \ \text{ since } Vn_A \simeq 4 \text{ (see main text)} \tag{69}$$

We conclude that with $k_{abs} \simeq 500\ \mathrm{s}^{-1}$, the probability for EEA to occur in a 30 wt%-loaded ONP is of order $4 \times 10^{-6}$. With $2 \times 10^6$ photons absorbed per second, we typically expect $\simeq 10$ EEA events per second per ONP, i.e. the photoproduction of 1 quencher state (i.e. EEA byproduct $Q$, see main text) per ONP every 5 seconds. For the 100 wt% loaded ONPs, the R18 dye density is 2.2 times larger, while $Vn_A = 2V/(\gamma\langle\tau\rangle)$ is essentially identical. This means that the rate of EEA events is about $2.2^2 = 5$ times larger in ONP100 than in ONP30, under identical cw light intensity.

# References


[1] A. Gharbi and J. Léonard, "EEA_Photolum," Apr. 2024. `https://hal.archives-ouvertes.fr/hal-04561022`.

[2] A. Dogariu, D. Vacar, and A. J. Heeger, "Picosecond time-resolved spectroscopy of the excited state in a soluble derivative of poly(phenylene vinylene): Origin of the bimolecular decay," *Physical Review B*, vol. 58, pp. 10218–10224, Oct. 1998. Number: 16.

[3] F. Fennel and S. Lochbrunner, "Exciton-exciton annihilation in a disordered molecular system by direct and multistep Förster transfer," *Physical Review B*, vol. 92, p. 140301, Oct. 2015.

[4] U. Gösele, M. Hauser, U. Klein, and R. Frey, "Diffusion and long-range energy transfer," *Chemical Physics Letters*, vol. 34, pp. 519–522, Aug. 1975.

[5] D. Zagier, "The dilogarithm function," in *Frontiers in Number Theory, Physics, and Geometry II: On Conformal Field Theories, Discrete Groups and Renormalization*, pp. 3–65, Springer, 2007.

[6] M. Kirm, V. Nagirnyi, E. Feldbach, M. De Grazia, B. Carré, H. Merdji, S. Guizard, G. Geoffroy, J. Gaudin, N. Fedorov, P. Martin, A. Vasil'ev, and A. Belsky, "Exciton-exciton interactions in CdWO 4 irradiated by intense femtosecond vacuum ultraviolet pulses," *Physical Review B*, vol. 79, p. 233103, June 2009. Number: 23.

[7] B. Valeur and M. N. Berberan-Santos, *Molecular fluorescence: principles and applications*. John Wiley & Sons, 2012.

[8] R. P. Haugland, "Handbook of fluorescent probes and research chemicals," *Molecular Probes, Eugene*, vol. 8, 1996.

[9] K. Trofymchuk, A. Reisch, P. Didier, F. Fras, P. Gilliot, Y. Mely, and A. S. Klymchenko, "Giant light-harvesting nanoantenna for single-molecule detection in ambient light," *Nature Photonics*, vol. 11, pp. 657–663, Oct. 2017.

[10] G. Beadie, M. Brindza, R. A. Flynn, A. Rosenberg, and J. S. Shirk, "Refractive index measurements of poly(methylmethacrylate) (pmma) from 04–16 $\mu$m," *Appl. Opt.*, vol. 54, p. F139, Nov. 2015.

[11] S. J. Strickler and R. A. Berg, "Relationship between Absorption Intensity and Fluorescence Lifetime of Molecules," *The Journal of Chemical Physics*, vol. 37, no. 4, pp. 814–822, 1962.

[12] D. Nettels, D. Haenni, S. Maillot, M. Gueye, A. Barth, V. Hirschfeld, C. G. Hubner, J. Léonard, and B. Schuler, "Excited-state annihilation reduces power dependence of single-molecule FRET experiments," *Phys. Chem. Chem. Phys.*, vol. 17, no. 48, pp. 32304–32315, 2015.

[13] A. Reisch, A. Runser, Y. Arntz, Y. Mély, and A. S. Klymchenko, "Charge-Controlled Nanoprecipitation as a Modular Approach to Ultrasmall Polymer Nanocarriers: Making Bright and Stable Nanoparticles," *ACS Nano*, vol. 9, pp. 5104–5116, May 2015. Number: 5.